Photocurrent spectroscopy of in-plane surface conductive diamond homostructures

Patrick Simon ●, Philipp Beck, Ankit Rathi ●, and Martin Stutzmann ●

Walter Schottky Institute, Physik-Department, Technische Universität München, Am Coulombwall 4, 85748 Garching, Germany

Jose A. Garrido[*]

Catalan Institute of Nanoscience and Nanotechnology (ICN2), CSIC, Barcelona Institute of Science and Technology,
Campus UAB, Bellaterra, Barcelona, Spain

Electrical breakdown at hydrogen/oxygen interfaces is limiting the use of nanoscaled diamond devices for the control of optically active defect centers. In this work electron transport across an oxygen-terminated potential barrier in a hydrogen-terminated surface conductive diamond is investigated. We analyze temperature-dependent current-voltage characteristics for different barrier widths and report on a reduced effective barrier height compared to theoretical expectations. This is ascribed to an inhomogeneous potential landscape, as observed by Kelvin probe and conductive force microscopy. Furthermore, we use photocurrent spectroscopy to discuss possible transport processes and identify a field dependent absorption feature. A defect state involved in transport across the barrier is proposed at the hydrogen-oxygen barrier approximately 1 eV above the valence band maximum. The new understanding enabled by our work may help to overcome the current limitations of diamond surface electronics.

I. INTRODUCTION

Diamond is a promising material with many outstanding features such as high thermal conductivity, high carrier mobility, high breakdown field, and chemical inertness, and it has been proposed to be used in the fields of biosensors as well as high power, high frequency devices [1–3]. Moreover, the silicon-vacancy and nitrogen-vacancy defect centers are considered promising candidates for future quantum computing applications [4]. Bulk diamond is a wide band gap semiconductor with a band gap of $E_{gap} = 5.47$ eV at 300 K [5]. After hydrogen termination, undoped single crystalline diamond exhibits a surface conductivity in air, which has been explained by the so-called transfer doping model [6]. A two-dimensional hole gas (2DHG) is formed just beneath the surface as a result of the upward bending of the conduction and valence bands induced by the C-H surface dipoles and subsequent equilibration of the Fermi level with atmospheric surface adsorbates [7]. In contrast, the oxygen-terminated diamond remains insulating because there are no feasible acceptor levels of surface adsorbates for electron charge transfer due to the opposite shift of the surface potential caused by the C-O dipole layer. Thus, selective surface oxidation leads to a lateral in-plane energy barrier of ≈2 eV for the 2DHG. In the past multiple electronic devices have been built on patterned devices such as solution-gated or in-plane gated field effect transistors and have been found to be useful tools to control and stabilize the charge state of defect centers [8–11].

However, parasitic current across the oxidized diamond and hysteresis effects limits the usability of these devices. In this paper, we investigate the current transport and defects present in these in-plane homostructures. We use photocurrent spectroscopy to identify relevant defect levels. In these measurements, we apply an electric field across a thin oxidized line acting as a potential barrier with a height of ≈2 eV [Fig. 1(c)], which modifies the band bending on the negatively biased side such that the Fermi level E_F is above the valence band maximum E_V close to the oxidized line, leading to a depletion of the 2DHG. Moreover, we evaluate the quality of the homostructure using Kelvin probe force microscopy (KPFM) and conductive atomic force microscopy (CAFM). Both techniques offer the possibility to map the potential landscape and the electric field on a microscopic level. In these measurements we find the potential along the interface to be surprisingly inhomogeneous, which induces additional defects. Finally, we use spectrally resolved photocurrent to identify the energetic position of these defect levels and observe a field-dependent blueshift of this absorption feature.

II. EXPERIMENTAL DETAILS

(100)-oriented, single crystalline, electronic grade diamond samples have been used in this work, with a specified nitrogen and boron background impurity concentration of below 5 ppb (Element Six. Ltd). Hydrogen termination was achieved in a quartz tube reactor (Seki Technotron Corp.) coupled to a microwave ASTEX plasma system at 750 W, 700 °C, and a H_2 flow of 100 sccm for 15 min, followed by a controlled cooldown at 230 W for 30 min. Conventional photolithography and electron beam lithography using a diluted ZEP520A
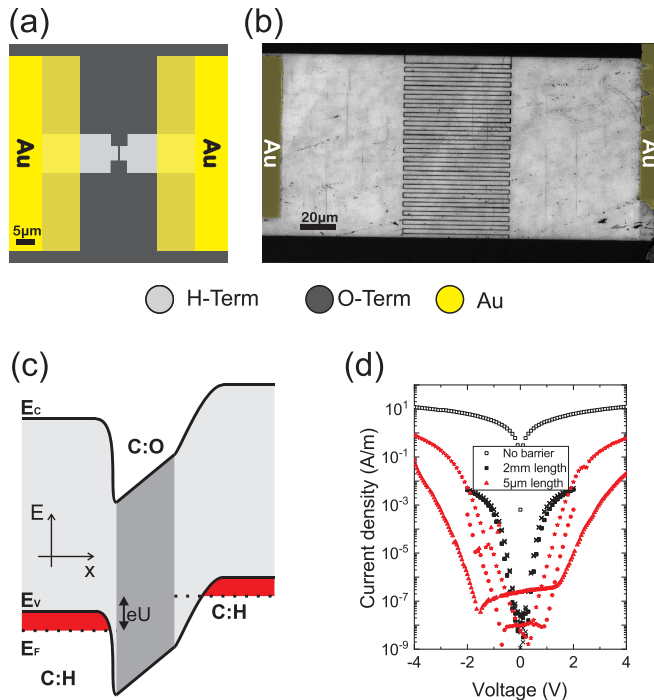
[*]joseantonio.garrido@icn2.cat

FIG. 1. Basic layout of the diamond in-plane homojunction. (a) Simplified structure of a conductive hydrogen-terminated channel interrupted by a thin oxidized barrier. (b) SEM image of a typical device layout. Hydrogen-terminated areas appear bright, whereas oxygen-terminated areas remain dark. (c) Band alignment in a patterned device. An electric field is applied across the insulating oxidized barrier, which causes the 2DHG to deplete at one side of the interface. (d) Current-voltage characteristics reached in five devices across a 300 nm wide barrier. Additionally, a device without an oxidized barrier is shown for comparison. The total interface length can be of 2 mm or 5 μm depending on the device. Different symbols represent different devices with the same nominal geometry.

resist with subsequent exposure to an oxygen microwave system are used to realize oxygen-/hydrogen-terminated homostructures on the hydrogen-terminated surface. Ohmic contacts are achieved by conventional photolithography and metal evaporation of Au overlapping with the hydrogen-terminated channel. All lithography steps were carried out under cleanroom conditions. Typical sheet carrier concentrations of 10^{13} cm^{-2} and Hall mobilities of 100 cm^2 V^{-1} s^{-1} are observed in these devices [12]. Controlled surface oxidation is either performed in an oxygen plasma dry etcher (Technics Plasma 100-E or Diener electronics Femto) or by ozonization using a Sander Lab ozonizator. An oxygen coverage of more than 0.25 monolayers is expected with this treatment, which is sufficient to completely suppress the surface conductivity of diamond [13,14]. Typical water contact angles of less than 5° indicate a high quality oxidation [15].

A simple device structure is sketched in Fig. 1(a). A 20 μm wide channel is contacted on both sides using Au metal contacts. A 5 μm long oxidized barrier is fabricated with widths between 100 nm and 500 nm. For photoelectrical characterization we increased the total interface length using an interdigitated structure in a 80 μm wide conductive channel as displayed in the SEM image shown in Fig. 1(b).

The hydrogen-terminated areas appear bright, whereas the oxygen-terminated areas remain dark. The gold contacts are colored to ease distinction to the oxygen termination. A 2 mm long interdigitated interface is created by a 300 nm wide well-defined oxidized line.

KPFM and CAFM measurements were performed using a Bruker MultiMode 8 atomic force microscope utilizing a Bruker "PFQNE-AL" Si probe or a TiN-coated Si probe (Golden Silicon Probes "FMG01/TiN"), respectively. For CAFM measurements the hydrogen-terminated areas are both contacted to the common ground of the AFM setup and an integrated voltage source applies a bias of up to 10 V between the tip and the diamond surface. However, Kelvin probe measurements are usually carried out without an additional in-plane bias. In order to achieve an additional lateral bias across the diamond junction, one side of the device was contacted to a common ground while the second side was contacted to an external voltage source (Keithley 2400) in series.

In order to obtain spectrally resolved photocurrents, the light of a 450 W Xenon lamp is passed through a Czerny-Turner monochromator (f/6.4) and a light chopper at a frequency of $\approx$7 Hz. The device is biased by a Keithley 617 electrometer and the resulting photocurrent is directly fed into a lock-in amplifier. The obtained current is then linearly normalized to the prerecorded spectrum of the light source. All measurements were carried out at room temperature and under ambient conditions if not stated otherwise.

III. RESULTS

We first investigate the current-voltage characteristics of the diamond devices in air without illumination. Figure 1(d) shows the corresponding voltage-current (UI) characteristics of five devices with an interface length of 2 mm or 5 μm for constant 300 nm wide oxidized lines. We observe an exponential current increase across the oxidized barrier at voltages well below 10 V. At a current level of above $\approx$1 μA, corresponding to the exponential current increase transitions into an ohmic behavior, which we tentatively attribute to a limitation by the access resistance of the channel leads. Moreover, we do not observe an abrupt change in conductivity as seen in classic dielectric breakdown but a continuous and reversible current increase. In order to get a figure of merit, we define a breakdown field at a current density of 200 μA m^{-1}, which is typically well below 0.5 MV cm^{-1} [16]. However, bulk diamond is postulated to be insulating for electric fields of more than 10 MV cm^{-1} and experimental values of up to 3 MV cm^{-1} have been reported for diamond Schottky devices [17]. Additionally, the average current density of the 2 mm long interface is several orders of magnitude larger compared to the 5 μm interface. This imbalance indicates not a homogeneous breakdown of the entire interface but rather the creation of multiple transport paths.

In order to identify the responsible current paths, UI curves of a single device were measured at temperatures between 150 K and 6 K in He atmosphere, which is shown in Fig. 2(a). A clear temperature dependence is observed, but the exponential voltage dependence remains constant. An Arrhenius plot of the current recorded at a fixed voltage of 1 V or 3 V is shown for devices with an interface length of
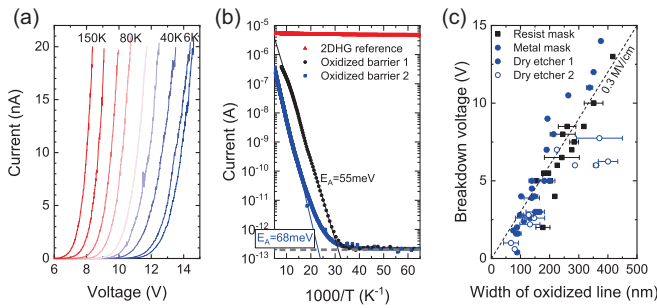
FIG. 2. (a) UI characteristics across a 300 nm wide barrier device for different temperatures. (b) Arrhenius plot of two similar devices with an interface length of 5 μm at a constant voltage of 3 V (black) and 2 mm at 1 V (blue). The dashed line indicates the noise limit and the solid line is a linear fit to the data. (c) Breakdown fields of numerous devices for different barrier widths and fabrication techniques.

5 μm or 2 mm, respectively in Fig. 2(b). With a decrease in temperature the current across the barrier drops exponentially with T^{-1} and is finally limited by the setup sensitivity limit of 10^{-13} A. In the same temperature range the current across a pure hydrogen-terminated conductive layer remains constant. Therefore, the overall conductivity variation is due to the current across the oxidized line. The main classical transport mechanisms that exhibit exponential UI characteristics and an Arrhenius dependence are the Poole-Frenkel effect and thermionic emission, which are both associated to charge carrier excitation from defects. For Poole-Frenkel transport the current is described by

$$I = we p_s \mu \frac{U}{d} \exp\left[\frac{-e}{kT}\left(\phi_B - \sqrt{\frac{eU}{\pi\varepsilon\varepsilon_0 d}}\right)\right], \qquad (1)$$

where w is the length of the interface, d the width of the barrier, p_s the sheet charge carrier concentration, μ the mobility, and $e\phi_B$ the barrier height of trap states above the valence band maximum [18,19]. For thermionic current a similar expression is used.

$$I = w A^{**} T^2 \exp\left[\frac{-e}{kT}\left(\phi_B - \sqrt{\frac{eU}{4\pi\varepsilon\varepsilon_0 d}}\right)\right], \qquad (2)$$

where A^{**} is the effective Richardson constant [5]. The potential barrier $e\phi_B$ can be determined from the slope of $\ln(I)$ or $\ln(IT^{-2})$, respectively. In our case the resulting values are around $e\phi_B \approx 150$ meV for Poole-Frenkel or $e\phi_B \approx 100$ meV for thermionic emission. Due to the similar nature of both mechanisms and good fits to the observed current no clear attribution can be made at the present time. However, both values are well below the expected barrier height of 2 eV. Hence, we propose that the potential landscape in the oxidized region is not as smooth as sketched in Fig. 1(c) but disturbed. This can either be due to incomplete oxidation or by surface defects generated during dry etching. Deep trap states within the oxidized barrier have already been reported in the past [20]. Both scenarios have the potential to lower the effective barrier height. For longer interface lengths the amount of surface defects is increased and closer to the expected value in case of a random distribution, whereas for short interfaces

the chance for a below average amount or even no defects is larger. This results in an increased amount of current paths through the interface and, thereby, an increased observable current. In order to get more insight into this observation we have evaluated numerous devices with the same nominal interface length but with different widths of the oxidized line and variations of fabrication techniques. Two different dry etching systems were used for oxidation and are referred to as dry etcher 1 and 2. In Fig. 2(c) the corresponding breakdown voltage (defined as the voltage for which a current level of 1 nA is reached) is plotted over the width of the oxidized line, which was determined by scanning electron microscopy (SEM) imaging. We observe a direct proportionality between barrier width and breakdown voltage, which corresponds to a breakdown field of ≈ 0.3 MV cm^{-1}. This correlation confirms a transport mechanism, where defects are equally distributed within the barrier and thereby reducing the effective potential barrier. Additionally, smaller barrier widths correlate with slightly lower breakdown fields whereas broader devices show this trend is reversed. This suggests an additional mechanism independent of the size of the oxidized area such as the roughness of the hydrogen-oxygen-terminated interface line, which could cause local field enhancements and thereby an overall reduced breakdown field. The impact of that effect becomes less noticeable for wider lines. Devices from different dry etching systems show an additional performance discrepancy, suggesting a different oxidation efficiency. This might be caused by different plasma geometry or cross contamination from previous users. Moreover, the oxidation efficiency can be further optimized by a preceding transfer of the resist pattern to a sacrificial metal layer, before dry etching instead of using the electron beam resist directly as a mask, for which the corresponding samples exhibit lower breakdown fields for all barrier widths. This performance increase can be explained that during dry etching the electron beam resist trench is etched and significantly broadens during the process. However, the initially covered parts of the trench receive a lower dose of oxygen radicals and might therefore not be completely oxidized, whereas a metal mask provides a robust barrier even for prolonged exposure to oxygen radicals.

In order to confirm the existence of an inhomogeneous electrical potential landscape, we use KPFM techniques to map the work function across the oxidized barrier. An AFM topology of the patterned diamond surface is shown in Fig. 3(a). Two 400 nm wide and ≈ 1 nm high vertical stripes, which correspond to the oxidized diamond lines on a hydrogen-terminated background, are shown on both sides of a surface crack. The height difference of the hydrogen and oxygen termination has been explained by the adsorbed water layer on the hydrophilic oxygen-terminated surface or an artifact by differences in frictional and adhesive forces [21,22]. In the KPFM image [Fig. 3(b)] a sharp potential increase between hydrogen- and oxygen-terminated areas is seen with a work function difference of up to 300 meV exceeding previously reported values of 100 meV [23]. However, within the oxygen-terminated area multiple potential drops of more than 100 mV can be observed as shown exemplary in a single slice across the oxidized line. This inhomogeneous potential landscape is expected to directly influence the effectiveness of the oxygen barrier, as it locally introduces additional trap
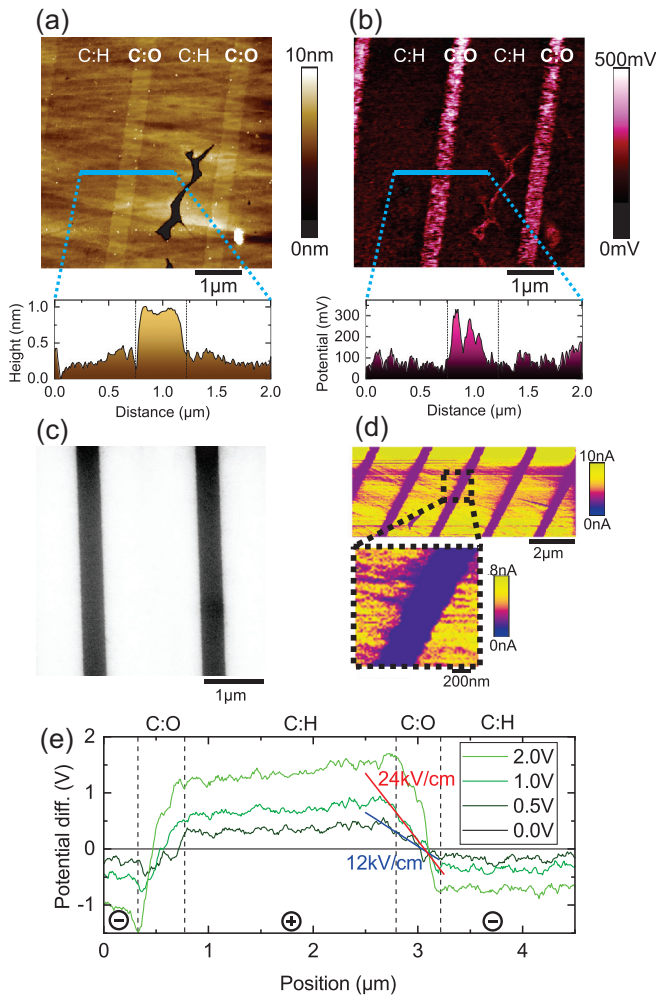
FIG. 3. Scanning probe microscopy images of an interdigitated diamond device. (a) AFM height map of two oxidized vertical stripes on a hydrogen-terminated background. A 1 nm height difference is observed, which is attributed to differences in hydrophobicity. (b) Simultaneously recorded KPFM potential map across the same device, revealing an inhomogeneous and fuzzy potential landscape in the oxidized barrier. (c) SEM image of a similar device. Oxygen-terminated areas appear dark; hydrogen-terminated areas appear bright, without the fuzziness of the KPFM image in (b). (d) CAFM map of a similar device showing five insulating oxidized stripes on a conductive hydrogen-terminated diamond. (e) Linear KPFM potential difference profiles across 400 nm oxidized lines with an additional lateral bias. The 0 V potential profile has been subtracted from all plots.

state-mediated transport mechanisms either through hopping or reduction of the overall barrier height. More importantly, the interface between hydrogen- and oxygen-termination appears rather rough, which is in direct contrast to the smooth appearance in AFM or SEM images [Fig. 3(c)].

These disturbances in the potential field have a direct impact on the microscopic band alignment and, ultimately, on the generation of the 2DHG. We use CAFM with a tip bias of 7 V to image these effects, which is displayed in Fig. 3(d). Within an overall conductive hydrogen-terminated region five insulating oxidized stripes are shown. Additionally, patterns

of lower conductance appear within the hydrogen-terminated region. Due to the structural similarities, we attribute these to polishing marks, which are also seen in the AFM image [Fig. 3(a)]. These additional surface defects may locally lower the mobility, reducing the conductance. A high resolution image of the oxidized barrier reveals a very rough interface, which is in good agreement with the rough potential landscape observed in the KPFM experiment.

In Fig. 3(b) the KPFM experiment was performed without any applied lateral bias, which is different from the devices typical operating conditions. When a negative bias is applied on one side of the barrier, the resulting field effect depletes the 2DHG on the other side. Moreover, an external field may charge or discharge defects, thereby changing the potential landscape. In order to investigate this phenomenon, we applied a lateral bias between two conductive hydrogen stripes in addition to the KPFM modulation. In Fig. 3(e) the potential change along such a cross section across two 400 nm wide oxygen-terminated barriers is shown in a bias voltage series between 0 V and +2 V. In this visualization the 0 V KPFM potential has been subtracted from all profiles in order to remove the superpositioned potential fluctuations due to the inhomogeneous oxidation (see Fig. S1 in the Supplemental Material [15]). Overall, the average potential offset between two adjacent conductive stripes corresponds well to the applied voltage. An overshoot that can be seen on the left side of the barrier is most likely a measurement artifact and corresponds to the right to left scan direction of the KPFM tip in the used retrace mode. Due to the sudden large potential increase the control algorithm shows a delayed reaction leading to an overestimation of the contact potential difference. This behavior has been observed in similar nanostructures [24]. Furthermore, an almost linear potential drop across the oxidized line can be observed as is shown exemplary for 0.5 V and 1 V on the right barrier and is in good agreement with the expected electric field of 25 kV cm^{-1} per 1 V bias voltage. Within the scope of our measurements we did not confirm major microscopic potential changes by biasing the device, suggesting that the device performance is stable and reproducible.

Spectrally resolved photoconductivity at room temperature has been used to gain further insight into the energy position of defects introduced during processing. As a control experiment we fabricated a fully oxygen-terminated diamond sample, contacted with interdigitated Ti/Au contacts at 10 μm spacing. The bias was chosen to achieve an electric field of 50 kV cm^{-1} for all devices. In the case of an unstructured oxygen-terminated diamond sample with a substitutional nitrogen concentration of $[N_S^0] < 5$ ppb and with an applied electric field of 50 kV cm^{-1}, the photocurrent abruptly rises by more than two orders of magnitude at photon energies above 5 eV and reaches its maximum at the band gap energy of 5.45 eV [Fig. 4(a)]. Above $\approx$5.2 eV a small shoulder is observed, which results from excitonic states with simultaneous absorption of a transversal optical and longitudinal acoustic phonon [25]. Below the band-to-band absorption a distinct shoulder appears at photon energies around 4.7 eV. A similar photocurrent feature has been attributed to nitrogen impurity related defects in the past [25–27]. We can conclude that the below gap absorption of nitrogen in the diamond substrates
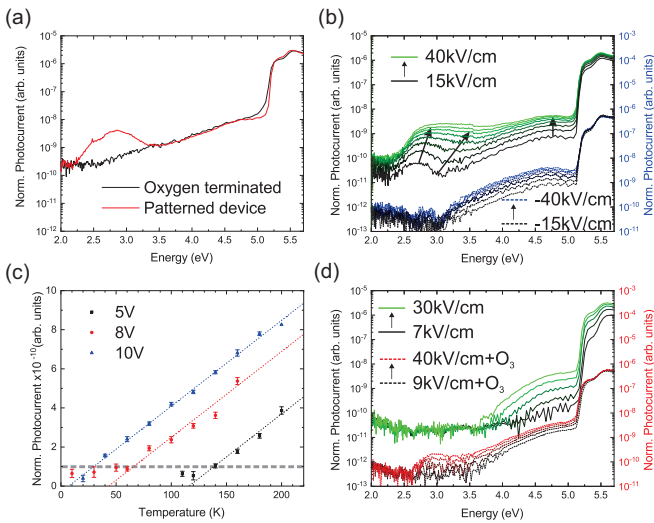
FIG. 4. Photocurrent spectra of hydrogen/oxygen-terminated diamond in-plane junctions fabricated using different material quality and surface treatments. (a) Ultra low nitrogen impurity ($[N_S^0] <$ 5 ppb) concentration at an electric field of 50 kV cm with a pure oxidized surface and after patterning of a surface conductive sample with an oxidized barrier. (b) Voltage series of an ultra low impurity device at positive (green) and negative (blue) voltages in ambient conditions. Black arrows indicate absorption shifts towards a larger bias. (c) Temperature dependence of the amplitude of the 2.7 eV absorption for different applied biases. The dashed line indicates the noise limit and dotted lines are a guide to the eye. (d) Photocurrent spectra of a diamond in vacuum as prepared and after 30 minutes of ozone treatment.

dominates the photocurrent spectra below $\hbar\omega = 5$ eV. After patterning a low impurity and hydrogen-terminated diamond with an oxygen barrier, an additional resonant absorption feature emerges at an energy of 2.7 eV, which is shown as the red spectrum in Fig. 4(a).

For further analysis we performed a bias series. When increasing the applied bias the photocurrent increases mainly linearly above photon energies of ≈ 4 eV, which is expected in the case of ohmic transport, with an observed superlinearity in the resonant absorption [15]. Furthermore, the resonant absorption at 2.7 eV starting with a FWHM of 0.3 eV at an electric field of 15 kV cm^{-1} broadens and shifts to higher energies with increasing electric fields as indicated by the black arrows in Fig. 4(b) and Fig. S3(b) in the Supplemental Material [15]. At an electric field of around 40 kV cm^{-1} the absorption maximum has shifted to 3.0 eV and broadened to a FWHM of 1.3 eV. When inverting the direction of the electric field, the absorption at 2.7 eV nearly vanishes, while the contribution by the nitrogen defect shoulder at 4.7 eV remains comparable, which is displayed by the blue spectra in Fig. 4(b). This asymmetry is in contrast to the symmetric device design and dark UI characteristics shown in Fig. 1(c). Upon reversal of the bias either the photogenerated charge carriers originating from a particular defect are trapped and recombine before reaching the electrodes or the excitation path is no longer possible, which will be discussed below.

A temperature analysis of the absorption feature at 2.7 eV yields a linear increase of the amplitude with temperature in

the range between 10 K and 200 K as shown in Fig. 4(c), which corresponds to a possible thermal energy below 2 meV. Typically, only classic Arrhenius dependence is reported in diamond photoconductivity [28,29]. The exact origin of this temperature dependence remains unclear, but it seems plausible that a broad distribution of defect energy levels can lead to a linear thermal dependence in photothermal ionization [30]. It is likely that such a broad distribution of defects is formed in the postulated random potential landscape of the interface and is confirmed by the measured FWHM of more than 1 eV.

In order to explain our experimental observations we propose a model where the absorption process is changed by an external field. Itoh *et al.* reported localized defects at the oxygen-hydrogen interface with energy levels between 2.0 eV and 2.4 eV [20]. From KPFM and CAFM imaging we have already shown that the potential landscape at the hydrogen/oxygen interface is rough and may, therefore, be an indicator for additional defect states. Additionally, even with low nitrogen impurity concentrations we still observe a significant photocurrent signal and can assume that the nitrogen defect takes part in the observed resonant photocurrent at 2.7 eV. We therefore estimate that the energy level of the defect is $E_1 \approx 1$ eV above the valence band at the oxygen-hydrogen interface using

$$E_1 = E_{\text{gap}} - E_{\text{nitrogen}} - 2.7 \text{ eV} \tag{3}$$

with E_{gap} the band gap of diamond and E_{nitrogen} the known defect level of nitrogen ≈ 1.5–1.7 eV below the conduction band [26]. This allows a photoionization path from the valence band to the defect level, then resonantly to the nitrogen defect level and finally to the conduction band. The observed asymmetry on the sign of the applied bias can be explained by the asymmetry of the interface at the oxidized barrier. The resulting microscopically different termination pattern may introduce different concentration and energetic levels of defects on both sides on the interface and makes complete electric depletion of those defects more feasible at one side. This result may appear as a discrepancy to the previously reported 100 meV effective potential barrier for dark equilibrium carriers in the contact regions. However, the formation of E_1 defects is a different manifestation of the disturbed potential landscape and corresponds to an optical excitation energy for carriers inside the barrier.

The blueshift is explained as follows. The quantum-confined Stark effect is known to cause a redshift [31], since the wave-function tail of the electrons and holes extends into the band gap and effectively lower the band-to-band transition energy. The model which we propose here is similar to a reversal of this process and is sketched in Fig. 5. When a bias is applied across the interface, the nitrogen defect band will be tilted accordingly. With a spatial separation between the E_1 defect and the nearest nitrogen defect the energy difference ΔE increases proportionally to the applied electric field. Assuming a spatial separation of 100 nm an energy increase of 0.4 eV is expected at an electric field of 40 kV cm^{-1}, which is in agreement with the experimentally observed blueshift. Furthermore, we experimentally confirmed a linear dependence between the electric field and the position of the absorption maximum [15].
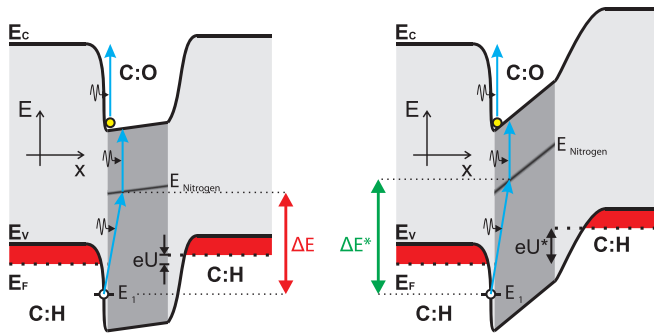
FIG. 5. Proposed model of the observed photocurrent absorption peak at 2.7 eV with a small applied voltage ($U \approx 0$; left) and large voltage ($U^* > 0$; right). An electron is resonantly excited from a defect generated at the oxygen-hydrogen-terminated interface ≈ 1 eV above E_V to the nitrogen defect level and is subsequently excited to E_C with an additional photon. Under external bias and for a spatial separation between interface defects and nitrogen impurities in the exposed layer a blueshifted absorption becomes possible.

Last but not least, we want to show that this defect state at $E_1 \approx E_V + 1$ eV is generated by oxidation of the surface, which occurs naturally during measurements and storage in ambient conditions. Figure 4(d) shows photocurrent experiments of a device for which the contact with air was minimized during fabrication by vacuum storage between fabrication steps. Additionally, the measurements were performed in vacuum as well to reduce the likelihood of unwanted oxidation. A device was selected where band-to-band transition, excitonic absorption, and the nitrogen-related defect absorption around 4.7 eV can still be clearly observed but without an additional absorption feature at 2.7 eV.

In order to achieve a mild and controlled oxidation, we exposed the entire device to 30 min of ozone and stored it in vacuum afterwards. After this treatment the dark conductivity across the junction dropped by two orders of magnitude, confirming additional oxidation of the surface. The corresponding photocurrent spectrum is shown in Fig. 4(d) (lower set of curves). Due to the reduced conductivity, the electric field had to be slightly increased. At an electric field of ≈ 20 kV cm^{-1} an absorption maximum with a 0.2 eV FWHM arises at an

energy level of ≈ 2.8 eV, which ultimately shifts to 3.0 eV at higher bias. This post-process defect formation is in good agreement with the previous results and confirms that surface oxidation is crucial for this defect level to be formed.

Similar surface defects attributed to partial hydrogenation or surface oxidation have been reported before at values of 1.6 eV or 1.78 eV above E_V, respectively [32,33]. However, the E_1 level is considerably closer to E_V and cannot be attributed to these defects in the literature, but a clear correlation with surface oxidation is evident.

IV. CONCLUSION

In summary, we have analyzed the electric behavior of an all diamond nanoscaled in-plane surface homostructure based on a hydrogen/oxygen terminated interface and observed a reduced effective barrier height in these devices compared to the theoretical prediction. Several microscopy techniques showed a smooth chemical surface but exhibited strong inhomogeneities in the electrical potential landscape across the surface. We complemented these results with photocurrent spectroscopy and identified a resonant absorption at $\hbar\omega \approx 2.7$ eV. We interpreted our findings by proposing a defect level at the interface approximately 1 eV above the valence band maximum and excitation to a nitrogen defect. Furthermore, we reported on a blueshift of this absorption feature proportional to the electric field that we explained by spatial separation of the defect and the nitrogen defect. Last but not least, we have shown that controlled oxidation can introduce this defect on a freshly fabricated device. Precise fabrication techniques, which provide sufficient and homogeneous oxidation of the surface combined with minimum exposure to the ambient environment, may further help to miniaturize diamond devices in the future.

[1] P. W. May, CVD diamond: A new technology for the future?, Endeavour **19**, 101 (1995).

[2] H. Taniuchi, H. Umezawa, T. Arima, M. Tachiki, and H. Kawarada, High-frequency performance of diamond field-effect transistor, IEEE Electron Device Lett. **22**, 390 (2001).

[3] T. Teraji, S. Koizumi, Y. Koide, and T. Ito, Electric field breakdown of lateral-type Schottky diodes formed on lightly doped homoepitaxial diamond, Appl. Surf. Sci. **254**, 6273 (2008).

[4] S. Prawer and A. D. Greentree, Applied physics. Diamond for quantum computing, Science (New York) **320**, 1601 (2008).

[5] S. M. Sze and K. K. Ng, *Physics of Semiconductor Devices*, 3rd ed. (Wiley-Interscience, Hoboken, NJ, 2007).

[6] F. Maier, M. Riedel, B. Mantel, J. Ristein, and L. Ley, Origin of Surface Conductivity in Diamond, Phys. Rev. Lett. **85**, 3472 (2000).

[7] M. V. Hauf, P. Simon, M. Seifert, A. W. Holleitner, M. Stutzmann, and J. A. Garrido, Low dimensionality of the surface conductivity of diamond, Phys. Rev. B **89**, 115426 (2014).

[8] H. Kawarada, Y. Araki, T. Sakai, T. Ogawa, and H. Umezawa, Electrolyte-Solution-Gate FETs Using Diamond Surface for Biocompatible Ion Sensors, Phys. Status Solidi A **185**, 79 (2001).

[9] A. D. Wieck and K. Ploog, In–plane–gated quantum wire transistor fabricated with directly written focused ion beams, Appl. Phys. Lett. **56**, 928 (1990).

[10] J. A. Garrido, C. E. Nebel, R. Todt, M.-C. Amann, O. A. Williams, R. Jackman, M. Nesládek, and M. Stutzmann, Novel in-plane gate devices on hydrogenated diamond surfaces, Phys. Status Solidi A **199**, 56 (2003).

[11] M. Pfender, N. Aslam, P. Simon, D. Antonov, G. Thiering, S. Burk, F. Fávaro de Oliveira, A. Denisenko, H. Fedder, J. Meijer, J. A. Garrido, A. Gali, T. Teraji, J. Isoya, M. W. Doherty, A. Alkauskas, A. Gallo, A. Grüneis, P. Neumann, and J. Wrachtrup, Protecting a Diamond Quantum Memory by Charge State Control, Nano Lett. **17**, 5931 (2017).

[12] C. E. Nebel, B. Rezek, D. Shin, and H. Watanabe, Surface electronic properties of H-terminated diamond in contact with adsorbates and electrolytes, Phys. Status Solidi A **203**, 3273 (2006).

[13] J. Zheng, X. Xie, A. Wee, and K. P. Loh, Oxygen-induced surface state on diamond (100), Diam. Relat. Mater. **10**, 500 (2001).

[14] P. Gluche, A. Aleksov, A. Vescan, W. Ebert, and E. Kohn, Diamond surface-channel FET structure with 200 V breakdown voltage, IEEE Electron Device Lett. **18**, 547 (1997).

[15] See Supplemental Material at http://link.aps.org/supplemental/10.1103/PhysRevB.101.205306 for contact angle measurements on hydrogen- and oxygen-terminated diamond, details of KPFM data, and a discussion on the energy shift and power dependence of the photocurrent absorption feature [34–43].

[16] We observe a matching UI characteristic in air, He atmosphere, and vacuum conditions .

[17] H. Umezawa, T. Saito, N. Tokuda, M. Ogura, S.-G. Ri, H. Yoshikawa, and S.-i. Shikata, Leakage current analysis of diamond Schottky barrier diode, Appl. Phys. Lett. **90**, 073506 (2007).

[18] J. R. Yeargan and H. L. Taylor, The Poole–Frenkel effect with compensation present, J. Appl. Phys. **39**, 5600 (1968).

[19] E. Arslan, S. Bütün, and E. Ozbay, Leakage current by Frenkel–Poole emission in Ni/Au Schottky contacts on Al0.83In0.17N/AlN/GaN heterostructures, Appl. Phys. Lett. **94**, 142106 (2009).

[20] Y. Itoh, Y. Sumikawa, H. Umezawa, and H. Kawarada, Trapping mechanism on oxygen-terminated diamond surfaces, Appl. Phys. Lett. **89**, 203503 (2006).

[21] K. Loh, X. Xie, Y. Lim, E. Teo, J. Zheng, and T. Ando, Surface oxygenation studies on (100)-oriented diamond using an atom beam source and local anodic oxidation, Surf. Sci. **505**, 93 (2002).

[22] Y. Kaibara, K. Sugata, M. Tachiki, H. Umezawa, and H. Kawarada, Control wettability of the hydrogen-terminated diamond surface and the oxidized diamond surface using an atomic force microscope, Diam. Relat. Mater. **12**, 560 (2003).

[23] M. Tachiki, Y. Kaibara, Y. Sumikawa, M. Shigeno, H. Kanazawa, T. Banno, K. Soup Song, H. Umezawa, and H. Kawarada, Characterization of locally modified diamond surface using Kelvin probe force microscope, Surf. Sci. **581**, 207 (2005).

[24] M. Hetzl, M. Kraut, T. Hoffmann, and M. Stutzmann, Polarity Control of Heteroepitaxial GaN Nanowires on Diamond, Nano Lett. **17**, 3582 (2017).

[25] E. Rohrer, C. E. Nebel, M. Stutzmann, A. Flöter, R. Zachai, X. Jiang, and C.-P. Klages, Photoconductivity of undoped, nitrogen- and boron-doped CVD- and synthetic diamond, Diam. Relat. Mater. **7**, 879 (1998).

[26] R. G. Farrer, On the substitutional nitrogen donor in diamond, Solid State Commun. **7**, 685 (1969).

[27] E. Rohrer, C. F. O. Graeff, R. Janssen, C. E. Nebel, M. Stutzmann, H. Güttler, and R. Zachai, Nitrogen-related dopant and defect states in CVD diamond, Phys. Rev. B **54**, 7874 (1996).

[28] C. E. Nebel, A. Waltenspiel, M. Stutzmann, M. Paul, and L. Schäfer, Persistent photocurrents in CVD diamond, Diam. Relat. Mater. **9**, 404 (2000).

[29] E. I. Lipatov, D. E. Genin, and V. F. Tarasenko, Pulsed photoconductivity in diamond upon quasi-continuous laser excitation at 222 nm at the formation of an electron–hole liquid, JETP Lett. **103**, 663 (2016).

[30] G. Bambakidis and G. J. Brown, Analysis of photothermal ionization spectra of shallow impurities in silicon, Phys. Rev. B **33**, 8180 (1986).

[31] D. A. B. Miller, D. S. Chemla, T. C. Damen, A. C. Gossard, W. Wiegmann, T. H. Wood, and C. A. Burrus, Band-Edge Electroabsorption in Quantum Well Structures: The Quantum-Confined Stark Effect, Phys. Rev. Lett. **53**, 2173 (1984).

[32] D. Takeuchi, C. E. Nebel, and S. Yamasaki, Surface defect states analysis on diamond by photoelectron emission yield experiments, Diam. Relat. Mater. **16**, 823 (2007).

[33] A. Stacey, N. Dontschuk, J.-P. Chou, D. A. Broadway, A. K. Schenk, M. J. Sear, J.-P. Tetienne, A. Hoffman, S. Prawer, C. I. Pakes, A. Tadich, N. P. de Leon, A. Gali, and L. C. L. Hollenberg, Evidence for primal sp^2 defects at the diamond surface: Candidates for electron trapping and noise sources, Adv. Mater. Interfaces **6**, 1801449 (2019).

[34] M. Nesládek, K. Meykens, K. Haenen, L. Stals, T. Teraji, and S. Koizumi, Photocurrent and optical absorption spectroscopic study of n-type phosphorus-doped CVD diamond, Diam. Relat. Mater. **8**, 882 (1999).

[35] C. E. Nebel, Electronic properties of CVD diamond, Semicond. Sci. Technol. **18**, S1 (2003).

[36] V. D. Mihailetchi, J. Wildeman, and P. W. M. Blom, Space-Charge Limited Photocurrent, Phys. Rev. Lett. **94**, 126602 (2005).

[37] M. Santamaria, S. Terracina, Y. Konno, H. Habazaki, and F. Di Quarto, Physicochemical characterization and photo-electrochemical analysis of iron oxide films, J. Solid State Electrochem. **17**, 3005 (2013).

[38] S. K. Mishra, S. Bayan, P. Chakraborty, and R. K. Srivastava, Defect-dominated optical emission and enhanced ultraviolet photoconductivity properties of ZnO nanorods synthesized by simple and catalyst-free approach, Appl. Phys. A **115**, 1193 (2014).

[39] P. P. Paskov, P. O. Holtz, B. Monemar, J. M. Garcia, W. V. Schoenfeld, and P. M. Petroff, Photoluminescence up-conversion in InAs/GaAs self-assembled quantum dots, Appl. Phys. Lett. **77**, 812 (2000).

[40] R. S. Chen, T. H. Yang, H. Y. Chen, L. C. Chen, K. H. Chen, Y. J. Yang, C. H. Su, and C. R. Lin, Photoconduction mechanism of oxygen sensitization in InN nanowires, Nanotechnology **22**, 425702 (2011).

[41] D. M. Tex, T. Ihara, I. Kamiya, and Y. Kanemitsu, Temperature and light-intensity dependence of upconverted photocurrent generation in shallow InAs quantum structures, Jpn. J. Appl. Phys. **53**, 05FV01 (2014).

[42] L. Ostrovskaya, V. Perevertailo, V. Ralchenko, A. Dementjev, and O. Loginova, Wettability and surface energy of oxidized and hydrogen plasma-treated diamond films, Diam. Relat. Mater. **11**, 845 (2002).

[43] M. Wang, N. Simon, C. Decorse-Pascanut, M. Bouttemy, A. Etcheberry, M. Li, R. Boukherroub, and S. Szunerits, Comparison of the chemical composition of boron-doped diamond surfaces upon different oxidation processes, Electrochim. Acta **54**, 5818 (2009).